International Journal of Mechanical Sciences 303 (2025) 110612

Contents lists available at ScienceDirect

International Journal of Mechanical Sciences

journal homepage: www.elsevier.com/locate/ijmecsci

Universal characteristics of local strain fields for creep failure prediction

Bakhtiyar Mammadli [a,*], Tero Mäkinen [b], Karol Frydrych [a,c], Panagiotis G. Asteris [d], Stefanos Papanikolaou [a]

[a] NOMATEN Centre of Excellence, National Center for Nuclear Research, ul. A. Soltana 7, 05-400 Swierk/Otwock, Poland
[b] Aalto University, Department of Applied Physics, PO Box 11000, 00076 Aalto, Espoo, Finland
[c] Institute of Fundamental Technological Research, Polish Academy of Sciences, Pawińskiego 5B, 02-106 Warsaw, Poland
[d] Computational Mechanics Laboratory, School of Pedagogical and Technological Education, Athens, Greece

ARTICLE INFO

Dataset link: https://doi.org/10.5281/zenodo.15554332

Keywords:
Creep
Digital Image Correlation
Local strain fields
Unsupervised machine learning
Dimensionality reduction techniques
Universal characteristics
Failure prediction

ABSTRACT

Material creep, defined as time-dependent strain accumulation under constant loading, can result in severe deformation and eventual component failure, posing a significant engineering challenge. Therefore, the possibility of early prediction of creep behavior is highly desirable. The objective of this study is to propose a robust method for predicting creep failure. To this end, we investigate the creep behavior of paper samples (quasi-brittle fiber composites) used as a model material, subjected to constant uniaxial tensile loads. Local strain fields are obtained through Digital Image Correlation and analyzed using dimensionality reduction techniques, a form of unsupervised machine learning, to identify universal indicators of deformation. This approach enables the detection of the onset of tertiary creep phase (deformation acceleration towards final failure), prediction of failure time, and accurate prediction of the failure location on the material surface just before the tertiary creep phase begins. Among the techniques used—Principal Component Analysis (PCA), Independent Component Analysis (ICA), Factor Analysis (FA), Non-negative Matrix Factorization (NMF), and Dictionary Learning (DL)—PCA and FA perform better in both detecting the onset of tertiary creep and predicting failure locations. The comparative analysis reveals the presence of universal characteristics in the evolution of local strain fields, offering a novel framework for studying material mechanics and providing key insights into failure prediction. In particular, the prediction of failure location as well as the comparison of the efficacy of various dimensionality reduction techniques are clearly novel aspects introduced in this work.

1. Introduction

Material creep [1] is an important phenomenon affecting the ability to predict long-term behavior of components made of various engineering materials, such as metals [2] or fiber-reinforced composites [3]. It is especially important when some components are expected to fulfill their function during many years of usage. E.g. nuclear power plants are expected to continuously operate for 60 years [4] or even more. Creep becomes even more crucial under accident scenarios, such as station blackout [5] or loss of coolant [6], where rapid and large creep deformation may occur due to elevated temperatures far beyond normal operating conditions.

Material creep continues to be an area of active research. Recent studies [7,8] have explored creep in Ni-based single crystal superalloys using models based on continuous damage mechanics and crystal plasticity. While the underlying modeling assumptions were similar, the focus of the papers was different. In Wen et al. [7], the effect of cooling holes on creep lives was assessed, and in Gu et al. [8], the model allowed for simulating creep behavior of single crystals with distinct crystallographic orientations and at various temperatures. Ni-based superalloy was also studied in Cheng et al. [9], where the creep-fatigue interactions were considered. This was motivated by rotating components being exposed to both steady loads (creep during dwell) and transient loads (fatigue during start-up/shut-down). This coupling of creep and fatigue has also been recently investigated by Mäkinen et al. [10].

Creep in fiber-reinforced polymer composites was analyzed in Li et al. [3]. Namely, the creep responses of both carbon fiber reinforced polymer (CFRP) and glass fiber reinforced polymer (GFRP) composites at room and increased temperature were studied in detail. The authors experimentallly determined the fractions of elastic, viscoelastic and viscoplastic deformation in the total creep strain response. CFRP composite appeared to have better creep resistance at room temperature. On the other hand, its creep properties decreased with increasing temperature to a much greater extent than in the case of the GFRP

* Corresponding author.
E-mail address: Bakhtiyar.Mammadli@ncbj.gov.pl (B. Mammadli).

https://doi.org/10.1016/j.ijmecsci.2025.110612
Received 12 November 2024; Received in revised form 14 July 2025; Accepted 15 July 2025
Available online 25 July 2025

composite. The fiber–matrix debonding was reported as a main creep failure mechanism. Qin et al. [11] performed molecular simulations in order to provide a deeper insight into the better creep resistance of CFRP as compared to GFRP composites at room temperature. Steered molecular dynamics simulations were carried out in order to understand the mechanism of fiber–matrix debonding (at room temperature). The observed higher creep resistance of CFRP could be explained by the shear thresholds hypothesis—the shear threshold appeared to be higher in the case of carbon fiber–matrix interphase than in the case of glass fiber–matrix interphase.

In metals that are not subjected to elevated temperature, creep proceeds extremely slowly and creep experiments can last for a very long time [12]. This has driven efforts to extrapolate short-term creep results at elevated stress or temperature to normal long-term conditions [13]. For instance in Ayubali et al. [14], a phenomenological model based on Arrhenius kinetics and the Monkman-Grant relationship was developed. The model allowed to predict long-term creep behavior based on short-term creep behavior. The model is suited for high temperature creep (up to 900 °C) and was tested for several different alloys. Arrhenius approaches have also been used to study the effects of material heterogeneity [15], as well as the deformation history [16] on the creep lifetimes.

Studying material creep from the fundamental science perspective is also possible using test materials. Paper [17] is an excellent test material because its macroscopic creep behavior — characterized by strain localization, damage accumulation, and abrupt failure — is qualitatively similar to that of many engineering materials, particularly quasi-brittle composites such as fiber-reinforced polymers and concrete. At the same time the creep rate in paper is much higher, enabling accelerated experiments and the use of full-field techniques such as DIC, cf. Koivisto et al. [18], where the lifetime of paper specimens was predicted using correlations between sample lifetime t_c and minimum creep rate time t_m; Mäkinen et al. [19], where tertiary creep in paper was analyzed using DIC; Mäkinen et al. [20], where the detection of the creep onset in paper was performed using principal component analysis (PCA); and Pournajar et al. [21], where both DIC and acoustic emission (AE) were applied to study creep in paper. The failure mode of paper [17] also shows qualitative resemblance to that of fiber-reinforced polymers [22] when examined via fracture surfaces, where fiber pull-out, bridging, and rough crack paths are commonly observed in both systems.

In the creep deformation of paper, three characteristic phases emerge: primary, secondary, and tertiary creep [18]. Initially, during primary creep, the global strain rate $\dot{\epsilon}$ decreases over time t according to the Andrade law [23], typically following a power-law relation of $\dot{\epsilon} \propto t^{-2/3}$, with the specific exponent value varying depending on the material. The secondary creep regime corresponds to logarithmic creep behavior [24], characterized by a strain rate decrease of $\dot{\epsilon} \propto t^{-1}$. This phase continues until the strain rate reaches its minimum. After the minimum, tertiary creep begins, characterized by an increase in strain rate in a power-law fashion. Previous studies and statistical analysis of numerous paper creep experiments have shown that in the sample geometry used here the time of minimum global strain rate occurs around 83% of the sample's lifetime and provides valuable insight into predicting the time of failure cf. Rosti et al. [25], where the spatial fluctuations in paper samples were studied, as well as the studies described above [18–20]. This predictive relationship is also known as the Monkman-Grant relationship in materials science [26]. Similar power-law (or logarithmic) creep behavior has been observed in e.g. many fiber-reinforced composite materials [27–31]. Despite the well-established understanding of global strain rate signal statistics, we present the results of our investigation on the creep deformation of paper through the analysis of local strain fields using dimensionality reduction techniques from an unsupervised machine learning perspective.

The progress of using artificial intelligence (AI) and machine learning (ML) in almost every domain of contemporary civilization is tremendous. The field of materials science and engineering is no exception to this rule, and several recent review papers illustrate this. Prakash and Sandfeld [32] discussed the opportunities and problems related to combining data science, informatics and materials science (thus forming a so called materials informatics domain). Rodrigues et al. [33] discussed applications of big data and machine learning in materials science. Pilania [34] provided an overview of successful applications of machine learning in materials science (including property predictions, materials design, aiding atomistic simulations and characterization, providing insights based on natural language processing etc.). The review by Frydrych et al. [35] focused on applications of materials informatics in the areas of mechanical deformation experiments and simulations. Finally, Papadimitriou et al. [36] discussed applications of artificial intelligence in the design, discovery and manufacturing of materials.

The progress of AI in materials science is ongoing. Recently, Benzaamia et al. [37] trained a deep learning (DL) architecture on externally bonded CFRP reinforced concrete column data. In order to ensure that the DL model provides physically sound and explainable results, additional monotonicity and smoothness criteria were enforced. They demonstrated that the trained DL model outperformed traditional models. One promising avenue is the development of so-called surrogate models that replicate computationally expensive simulations. For example, Deshpande et al. [38] developed a surrogate model for non-linear finite element simulations allowing for the prediction of the deformation field of a body subjected to external loading. Wang et al. [39] developed a surrogate model for prediction of damage and lifetime in components resulting from creep and fatigue. The developed methodology was demonstrated on two examples, namely the elbow pipe made of austenitic stainless steel 316 L and the hydrogenation reactor made of chromium-molybdenum 2.25Cr1Mo steel. Creep-fatigue interactions were also the subject of a study by Liu et al. [40]. The model developed by them was used to perform FE simulations of turbine blades made of SiC/SiC composite.

Of course, AI and ML work best when there is a vast amount of data. Digital image correlation [41] is an example of a technique that produces large amount of data, since at each pixel there is information about each surface strain component. This is why one particularly useful approach of using ML in materials science is combining it with DIC. For instance Leygue et al. [42] used inhomogeneous strain data obtained from DIC to data driven computational mechanics [43]. Cidade et al. [44] managed to determine dynamic fracture toughness in carbon fiber reinforced epoxy composites using DIC data and ML. Rezaie et al. [45] developed a DL method for crack segmentation using DIC images. The method was demonstrated on experimentally obtained grayscale images of stone masonry walls subjected to various loading conditions. Image segmentation using DIC was also performed in Perera et al. [46], where the surface of a reinforced concrete beam (strengthened with externally bonded FRP composite plate) was divided into two regions (damage/no damage) using the methodology relying on PCA and k-means clustering.

There have also been attempts to replace traditional DIC algorithms with DL. One such attempt was reported in Min et al. [47], where the displacement field was obtained using a convolutional neural network (CNN). Boukhtache et al. [48] applied a CNN in order to retrieve subpixel displacement fields, thus being an alternative to classical subset-based DIC. Yang et al. [49] developed the deep DIC framework, in which two separate CNNs were trained to infer displacement and strain fields from deformed sample images. The model was trained on synthetic data and tested on data from real experiments. Applications of DL models for DIC were reviewed by Archana and Jeevaraj [50]. Using unsupervised learning for a similar task was also recently reported by Cheng et al. [51].

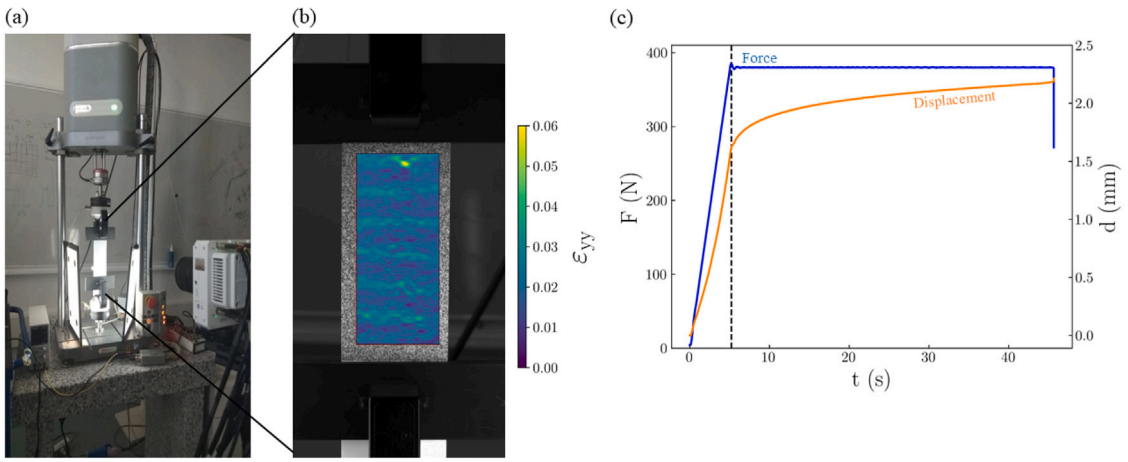

Fig. 1. (a) An image of the experimental setup, with a high-speed camera positioned in front of the testing machine. Illumination is achieved using two LED light panels. (b) Strain map at the last second of the sample's lifetime, overlaid onto the reference image within the designated ROI (Region of Interest). (c) The raw data extracted from the tensile testing machine depicts a stress-controlled experiment. It commences with an initial stress ramp lasting 5.23 s, succeeded by a constant load of $F = 380\,\mathrm{N}$ until the sample's failure at $t = 45.7\,\mathrm{s}$ (depicted in blue on the left axis). The measured total displacement d exhibits a characteristic creep curve, demonstrating an increase in strain (decrease in strain rate) while keeping the load constant (depicted in orange on the right axis).

In our study, we demonstrate the effectiveness of dimensionality reduction techniques as unsupervised machine learning methods for analyzing DIC data to study material creep behavior. Using PCA as a primary dimensionality reduction technique, we identify the optimal range of strain maps for detecting tertiary creep onset (the time of minimum global strain rate, $t_{\min}$) and apply this range to other techniques, including Non-negative Matrix Factorization (NMF), Factor Analysis (FA), Independent Component Analysis (ICA), and Dictionary Learning (DL). A comparison across these techniques reveals a universal characteristic in the evolution of local strain fields, serving as a reliable precursor for predicting failure time. We also demonstrate the ability to capture characteristic images (referred to as "component maps") of the strain map evolution using these dimensionality reduction techniques. By applying PCA, FA, and ICA to a specific range of strain maps close to the tertiary creep phase, we achieve accurate predictions of the failure location. Finally, we present a method for evaluating and selecting the optimal dimensionality reduction techniques by reconstructing strain maps from dimensionally reduced spaces and comparing them with the original strain maps.

The article is structured as follows. After this introductory section, the *Methods* section describes both the experimental setup and the computational approach. Next, the *Results* section presents the findings from applying various dimensionality reduction techniques to the data. The *Discussion* section analyzes the key results and discusses the current limitations and perspectives of the study. The article concludes with the *Conclusions*, which summarize the main findings and outline potential future applications of the developed approach.

2. Methods

The present section is divided into two subsections. The first describes the experimental procedure applied. The second summarizes data preprocessing and all the dimensionality reduction techniques that have been used.

2.1. Experiment

In this section, we outline the details of our experimental approach. As illustrated in Fig. 1a, the setup involved using the Instron ElectroPuls E1000 tensile testing machine, which applied a constant load F to the marked sample at the center while recording the piston displacement d. The global strain (ε) was determined using the formula $\varepsilon = \frac{d}{h}$, with h representing the specimen's initial height. Additionally, the Phantom S990 high-speed camera captured images of the samples at a resolution of 26.7 μm/pixel and a frequency of 30 Hz. The paper samples, sized 69 mm × 142 mm and with a grammage of 75 g/m^2, were printed with a random speckle pattern.

During the experiments, the tensile testing machine applied a constant load of 380 N. This load was selected as it represents 90% of the average load that caused failure in five preliminary test samples and was used consistently across all experiments. The application of this constant load was controlled via a linear load ramp over a duration of 5 s.

The results discussed are based on four experiments, with sample lifetimes varying from 23 s to 145 s. These experiments were chosen to ensure that each sample's lifetime was longer than the time required to ramp up to the constant stress level.

The DIC analysis is conducted using the AL-DIC software [52]. We first select the specific area from the surface image of the sample, which is called Region of Interest (ROI). The selection of the ROI is done by including most of the sample gauge area, but excluding a small portion around the edges to avoid edge effects in the DIC calculations (see Fig. 1b). After the determination of ROI area, the software calculates local displacements $\mathbf{u} = (u, v)$ relative to the first image, employing circular subsets with a radius of 3.7 mm. Subsets are placed every 26.7 μm. The local strain component in the loading direction, denoted as ϵ_{yy}, is then computed from these displacements as $\epsilon_{yy} = \frac{\partial v}{\partial y}$ using simple finite difference numerical differentiation. The resulting strain field is represented by an array of 801 pixels in width and 1841 pixels in height.

We employ an outlier-removal process to the DIC strain fields by considering each timeseries $\epsilon_{yy}(x, y)$, for a single x and y, and removing clear outliers (points that deviate more than three scaled median absolute deviations from the median). These outliers are set to the mean values of the previous and next values. We additionally require that the strains increase monotonously. This is done by constructing a monotonously increasing upper and lower envelope of the strain timeseries and taking their average to correspond to the strain [53].

We also consider the scale of the DIC analysis relative to the characteristic structural scale observed in paper, with a specific focus on flocs. Flocs, clusters of fibers formed during papermaking, are integral to the visible cloudiness observed in the paper structure. According to literature [17], this structural scale typically measures around 2 mm.

2.2. Dimensionality Reduction (DR) analysis

The following subsections contain details about data preprocessing and all the dimensionality reduction techniques applied, namely: principal component analysis, non-negative matrix factorization, factor analysis, independent component analysis and dictionary learning.

2.2.1. Data preprocessing

We begin by considering the computed strain fields $\epsilon_{yy}^{(k,i)}$, where the index i traverses all V spatial points, and k represents the time step. These strain fields undergo a normalization process, producing a matrix X with normalized input vectors as rows:

$$X_{(k,i)} = \frac{|\epsilon_{yy}^{(k,i)} - \langle \epsilon_{yy}^{(k,i)} \rangle|}{\sqrt{\langle (\epsilon_{yy}^{(k,i)})^2 \rangle - \langle \epsilon_{yy}^{(k,i)} \rangle^2}}, \tag{1}$$

where $\langle \cdot \rangle$ denotes spatial averaging. This normalization procedure first subtracts the spatial mean from each strain field and then applies the absolute value to focus on the magnitude of strain deviations, ensuring that both positive and negative fluctuations from the mean are treated equally, while maintaining unit variance. By emphasizing the intensity of strain changes, this approach ensures that the data is well-prepared to identify critical trends in the deformation process, serving as robust input for the Dimensionality Reduction techniques.

2.2.2. Principal component analysis (PCA)

After the data preprocessing steps, we proceed with principal component analysis (PCA) [54] to extract the principal components from the strain fields that capture most of the variability in the data [55–57]. The process involves the singular value decomposition of the matrix X, represented as

$$X = U \Sigma W^{\mathrm{T}}. \tag{2}$$

Here, U contains the left singular vectors, W contains the right singular vectors, and Σ is a diagonal matrix containing the singular values of X. Each singular value σ_j corresponds to a principal vector s_j.

To capture variations in the data, we compute the eigenvalues λ of the covariance matrix C for the input vectors using the formula:

$$C = \frac{X^{\mathrm{T}} X}{n-1} = U \left(\frac{\Sigma^2}{n-1} \right) U^{\mathrm{T}}. \tag{3}$$

Here, n represents the number of samples corresponding to the number of strain maps as rows of matrix X. The singular values σ_j are linked to the eigenvalues λ_j through the relation $\sigma_j = \sqrt{\lambda_j (n-1)}$.

We compute the projection of the principal components onto the strain maps:

$$\mathrm{PCA}_j^k = \frac{s_j \cdot X_k}{\sqrt{\sigma_j}}, \tag{4}$$

where X_k is the strain map at the kth time step, and s_j denotes the jth principal vector.

The principal vectors s_j are reshaped to match the size of the original strain maps, creating "component maps" that illustrate the spatial distribution of each principal component across all spatial points.

Finally, for data reconstruction, we use the following equation:

$$\hat{X}_k = \sum_{j=1}^{n} \mathrm{PCA}_j^k \cdot s_j \cdot \sqrt{\sigma_j}, \tag{5}$$

where $\hat{X}_k$ is the reconstructed strain map at time step k, using the top n principal components.

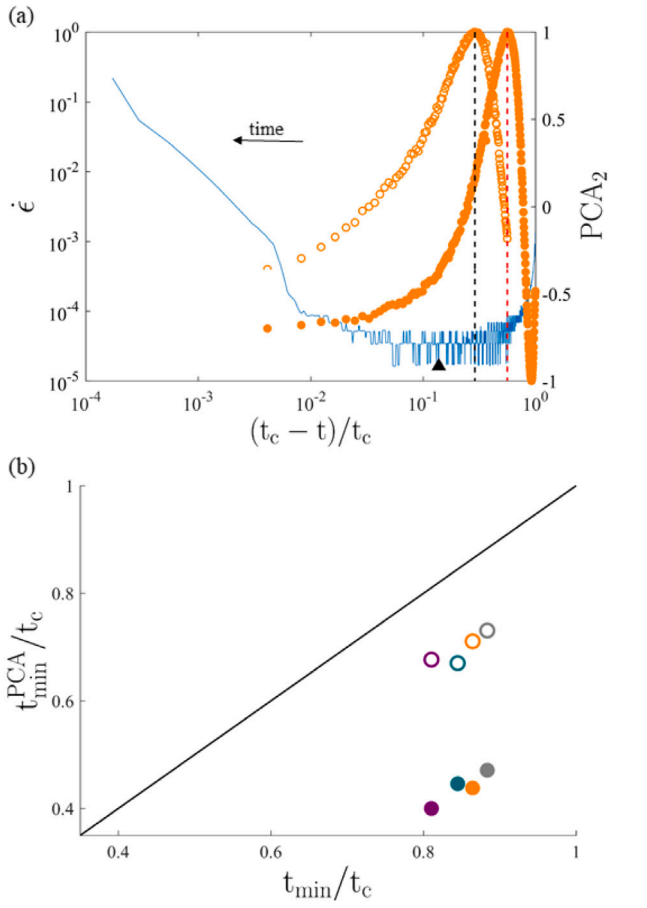

Fig. 2. Improvement of the PCA detection of the minimum strain rate time (t_{min}). (a) Global strain rate ($\dot{\epsilon}$) curve for a representative experiment (left y-axis, blue curve) and the corresponding second PCA component projection (right y-axis, orange curves) plotted against the normalized time before failure $(t_c - t)/t_c$ (bottom), where t_c denotes the failure time. The filled circles represent the second PCA component projection derived from the strain maps spanning from the onset of primary creep until the point of failure. The peak location of these component projection serves as the starting index for a new PCA analysis (indicated by empty circles) of the same experiment, resulting in an improved detection approach with the peak location converging towards t_{min} (indicated with a black triangle marker on the global strain rate curve). (b) Peak location of the second PCA component projection, t_{min}^{PCA} [Eq. (15)], plotted against the time of minimum strain rate, t_{min}. The filled markers represent the peak location of the component projection derived from the entire creep deformation region, while empty markers represent the detection of t_{min} using component projection from improved PCA analysis (the case of the curve with empty circles in panel (a)). Colors of the empty and filled markers are consistent across the experiments. The black line corresponds to the case where $t_{min}^{PCA} = t_{min}$.

2.2.3. Non-negative matrix factorization (NMF)

Non-negative matrix factorization (NMF) [58] is a dimensionality reduction technique that factorizes a non-negative data matrix X into two lower-dimensional matrices, W and H, where all elements are non-negative [59,60]. In the context of analyzing strain maps, NMF extracts spatial patterns in a way that allows the coefficients to be non-negative, aiding in the interpretability of the results.

Starting with the normalized strain maps in matrix X, NMF seeks to approximate X as the product:

$$X \approx W \cdot H, \tag{6}$$

where W represents the basis components (patterns), and H represents the activation matrix indicating the presence of these components in each strain map.

The resulting W matrix contains the spatial patterns, while the H matrix provides the corresponding NMF coefficients. For better notation

clarity, we denote the coefficients as NMF_j^k, which represent the contribution of the jth basis component to the strain map at the kth time step.

The "component maps" are derived by reshaping the columns of W to match the size of the original strain maps, providing visual representations of the identified spatial patterns.

For the reconstruction of the strain maps, we use the following equation:

$$\hat{X}_k = \sum_{j=1}^{n} NMF_j^k \cdot W_j, \tag{7}$$

where $\hat{X}_k$ is the reconstructed strain map at time step k, and n denotes the number of NMF basis components used in the reconstruction.

2.2.4. Factor Analysis (FA)

Factor analysis (FA) [61] is a method that explores the underlying factors influencing observed variables and captures their interrelationships [62,63]. Post data preprocessing, factor analysis involves estimating the factor loading vectors and unique variances.

The factor loading matrix L is determined by solving the equation

$$X = LF + E, \tag{8}$$

where X is the data matrix (comprising strain maps in rows), F is the factor score matrix, and E is the matrix of unique variances. The goal is to obtain L such that E is minimized. The factor loading vectors represent the weights of each factor for each strain map.

To obtain the factor scores, we project the input vectors (strain maps) onto the factor loading vectors as follows:

$$FA_j^k = X_k \cdot L_j^{\mathrm{T}}. \tag{9}$$

Here, FA_j^k represents the factor score for the jth factor at the kth time step, capturing the contribution of that factor to the strain map at time step k.

After obtaining the factor loading vectors, we reshape them to match the size of the original strain maps, producing "component maps" that illustrate the spatial distribution of each factor's influence across all spatial points.

Finally, the reconstruction of the strain maps from FA can be expressed as:

$$\hat{X}_k = \sum_{j=1}^{n} FA_j^k \cdot L_j, \tag{10}$$

where $\hat{X}_k$ is the reconstructed strain map at time step k using the top n factors.

2.2.5. Independent component analysis (ICA)

Independent component analysis (ICA) [64] is a technique that separates a multivariate signal into additive, independent components [65]. In the context of dimensionality reduction for strain maps, ICA aims to identify spatial patterns that are statistically independent.

The objective is to find a matrix W that satisfies the equation

$$ICA_j^k = X_k \cdot W_j^{\mathrm{T}}. \tag{11}$$

In this equation, ICA_j^k represents the projection of the jth independent component for the strain map at the kth time step. The columns of matrix W contain components assigned to each strain map for a specific independent component.

ICA is particularly useful when the assumption of statistical independence among components is valid. After obtaining the matrix W, each column of W represents a spatial pattern that is statistically independent from the others. These spatial patterns are reshaped to match the size of the original strain maps, forming "component maps".

Finally, for reconstruction, the input data can be reconstructed using the inverse transformation:

$$\hat{X}_k = \sum_{j=1}^{n} ICA_j^k \cdot W_j, \tag{12}$$

where $\hat{X}_k$ represents the reconstructed strain map at time step k, and n is the number of independent components.

2.2.6. Dictionary Learning (DL)

Dictionary learning [66] is a versatile technique for representing data as a linear combination of atoms from a learned dictionary [67]. In the context of strain maps, dictionary learning aims to find a sparse representation of the input data, capturing essential patterns and features.

Starting with the normalized strain maps in matrix X, dictionary learning seeks to express each strain map as a sparse linear combination of basis elements from a dictionary matrix D. Mathematically, this is represented as:

$$X \approx D \cdot A, \tag{13}$$

where A is a sparse coefficient matrix. The columns of the matrix D are the basis elements or atoms, and the sparse coefficients A provide insights into the importance of each basis element for a specific strain map. Through iterative updates to D and A, the algorithm refines the dictionary to capture the most salient features of the strain maps.

For clarity, we introduce dictionary learning (DL) coefficients, denoted as DL_j^k, which represent the contribution of the jth basis element to the strain map at the kth time step.

In this method, we refer to the "component maps" as the columns of the dictionary matrix D, which can be reshaped to match the size of the original strain maps. The component maps offer insights into the spatial distribution and importance of each basis element across all spatial points.

For data reconstruction, we use the following equation:

$$\hat{X}_k = \sum_{j=1}^{n} DL_j^k \cdot D_j, \tag{14}$$

where $\hat{X}_k$ is the reconstructed strain map at time step k, using the top n basis elements from the dictionary.

At the end of the Dimensionality Reduction (DR) Analysis section, we introduce the term "component weight", referring to the projection, coefficient, or score of the components, depending on the specific DR technique used. For simplicity, the abbreviation of each DR technique's name is used to denote its respective component weight. We summarize that the DR techniques are employed to extract components, with their associated component weight plotted as time series to help detect the onset of tertiary creep, a critical transition in the deformation process. Additionally, these components are used to create "component maps", providing spatial insights into the deformation patterns leading up to failure. The DR techniques are also used to reconstruct the strain maps, enabling an assessment of each technique's accuracy by analyzing the mean and standard deviation of the differences between the original and reconstructed maps.

3. Results

The present section is divided into three subsections. First, we present the detection of the tertiary creep onset based on the evolution of the component weights obtained from dimensionality reduction techniques. Then, we discuss the prediction of the failure location using component maps derived from the same techniques. Finally, we provide a comparative assessment of the different methods to evaluate their performance.

Table 1
Time of the minimum of the global strain rate signal, t_{min}, and its detection using the analysis of the local strain fields with five dimensionality reduction techniques. All values are divided by the time of failure, t_c. The last three columns indicate the average values across the four tests, with the standard deviation (STD) and coefficient of variation (CV) computed based on those averages.

	Test 1	Test 2	Test 3	Test 4	Average	STD	CV (%)
t_{min}/t_c	0.8644	0.8835	0.8448	0.8104	0.8508	0.0305	3.58
PCA	0.7107	0.7273	0.6716	0.6959	0.7014	0.0225	3.20
NMF	0.7107	0.7273	0.6716	0.7242	0.7084	0.0246	3.48
FA	0.7107	0.7273	0.6865	0.6818	0.7016	0.0195	2.78
ICA	0.6736	0.6653	0.6087	0.6393	0.6467	0.0274	4.24
DL	0.6901	0.7397	0.7056	0.7242	0.7150	0.0209	2.92

3.1. Detection of tertiary creep onset

In the paper creep experiments, we encountered excessively noisy global strain rate signals. To enhance the clarity of the data, we applied noise reduction techniques by utilizing a moving average of the strain with a small time interval. An example demonstrating the global strain rate signal is presented in Fig. 2 a (left y-axis). Here, we observe the characteristic creep behavior: a decrease in strain rate during the primary creep phase, followed by a period of relatively constant fluctuating signals, which would correspond to the secondary creep regime. Finally, we observe an acceleration towards failure in a power-law fashion, indicative of the tertiary creep regime. However, it is important to note that in a highly noisy signal, precisely determining the region of secondary creep (which is often very small in the case of paper creep deformation) and identifying the minimum of the global strain rate curve is significantly challenging. One sensible approach that we used to determine the minimum strain rate is by employing a larger averaging window. By systematically increasing the averaging window size across the tests, we observed that after a certain threshold the global strain rate signal consistently exhibited a single clear minimum without noise-induced fluctuations, and the detected t_{min} remained unchanged with further increases in window size, allowing for a robust identification of t_{min}. A detailed analysis of this methodology and the impact of different averaging window sizes is provided in Appendix. However, for visualization of creep behavior, smaller window sizes were used to better demonstrate creep stages. In highly noise-reduced signals, we then identify the minimum and its corresponding time, which would correspond to the onset of tertiary creep. After determining the minimum strain rate time (t_{min}) from global strain rate signal, we compare it with the detected time for tertiary creep onset from the dimensionality reduction analysis of the local strain fields.

We demonstrate the capability to capture the essential characteristics of local strain field evolution through dimensionality reduction analysis applied to the matrix containing all strain maps during deformation. Principal Component Analysis (PCA) serves as an illustrative example, identifying orthogonal components that capture the most variability in the DIC strain fields. By utilizing the strain maps from the onset of primary creep until failure (Fig. 2a), we observe that the second PCA component projection shows a clear peak around the point where global strain rate signals start to plateau, would correspond to the onset of the secondary creep regime. However, our primary goal is to define the onset of tertiary creep (the time of minimum global strain rate, t_{min}) as a failure precursor. Therefore, we discard the strain maps before the peak location of the second PCA component projection and select strain maps from the detected secondary creep onset until failure for a new PCA analysis. As a result, we observe a peak on the second PCA component projection around the time of minimum global strain rate, which corresponds to the onset of tertiary creep. We refer to this approach as the "improved PCA analysis" for the detection of tertiary creep onset, as it involves using a specific range of strain maps determined by the PCA analysis. We then define the following relation:

$$t_{min}^{PCA} = \arg\max PCA_2. \tag{15}$$

In Fig. 2b, across all the experiments, we observe that the results of the PCA analysis that utilize the strain maps from the whole creep deformation region (indicated with filled circles) exhibit more scatter from the detected time of tertiary creep onset (t_{min}) from global strain rate signals. Nonetheless, it is noteworthy that all these time points that correspond to the beginning of the plateau on the global strain rate signals, correspond to the onset of secondary creep. However, the results of the improved PCA analysis (indicated with empty circles) consistently approach the time of minimum global strain rate signals which detect the tertiary creep onset.

We utilized the same range of strain maps that were used in the improved PCA analysis for detecting the onset of tertiary creep (refer to Fig. 2) as input for the other dimensionality reduction techniques. This is demonstrated in Fig. 3, which shows the component weight of all methods across three components. At first glance, we observe that the components weight of three methods (PCA, NMF, and DL) exhibit consistent behavior across all tests. However, for FA and ICA, the components weight may vary depending on the specific test. In cases where the tests display consistent behavior, we note that the third NMF (Fig. 3f) and first DL (Fig. 3m) components coefficient show a clear peak around the peak location of the second PCA component projection (Fig. 3b), occurring near the time of minimum strain rate. Subsequently, we define the following equations for the detection of t_{min} using NMF and DL components coefficient, similar to Eq. (15):

$$t_{min}^{NMF} = \arg\max NMF_3 \tag{16}$$

and

$$t_{min}^{DL} = \arg\max DL_1. \tag{17}$$

For the second FA (Fig. 3h) and first ICA (Fig. 3j) components weight, we observe a minimum around the maximum peak position of the components weight from other methods (those used to detect t_{min}) in three out of the four tests. The exception occurs in Test 3, where the third FA component score (Fig. 3i) also shows a similar behavior. However, in Test 1, the second ICA component projection (Fig. 3k) shows a maximum around the detected t_{min}.

After obtaining the definitions [Eqs. (15), (16), (17)] for PCA, NMF, and DL for the detection of t_{min}, and considering the cases of FA and ICA, including their respective minimum peaks of the second and first components weight (including exceptional cases), we present the results in Table 1. The table shows the detected t_{min} values from DIC strain fields and global strain rate signals as the ratio t_{min}/t_c, normalized by the failure time t_c. The dimensionality reduction techniques generally outperform the global strain rate signals in detecting the onset of tertiary creep, as the global strain rate case exhibits a higher standard deviation. Additionally, in some tests, the results of PCA, NMF, and FA are identical, suggesting a potential universal characteristic in the evolution of strain fields.

The table also highlights the consistency of the dimensionality reduction techniques in detecting t_{min}. PCA, FA, and DL demonstrate closely aligned results with lower variability, whereas NMF and ICA exhibit more variation, as indicated by their higher standard deviations (STD) and coefficients of variation (CV) computed based on the average values across four tests. ICA, in particular, has the highest standard deviation, indicating it may be more sensitive to noise or component selection. A detailed analysis of the causes behind the observed variability among the different techniques, particularly for ICA and NMF, is provided in Section 3.3. Overall, the average t_{min}/t_c across all DR techniques remains relatively close, suggesting each method is capable of identifying the critical point of deformation.

By further examining Fig. 3, we can provide additional insights into the remaining components weight of the methods. Regarding the PCA components projection, we observe that the first PCA component projection (Fig. 3a) transitions from a low value to a high constant value around the peak position of the second PCA component projection (Fig. 3b). Additionally, the third PCA component projection (Fig.

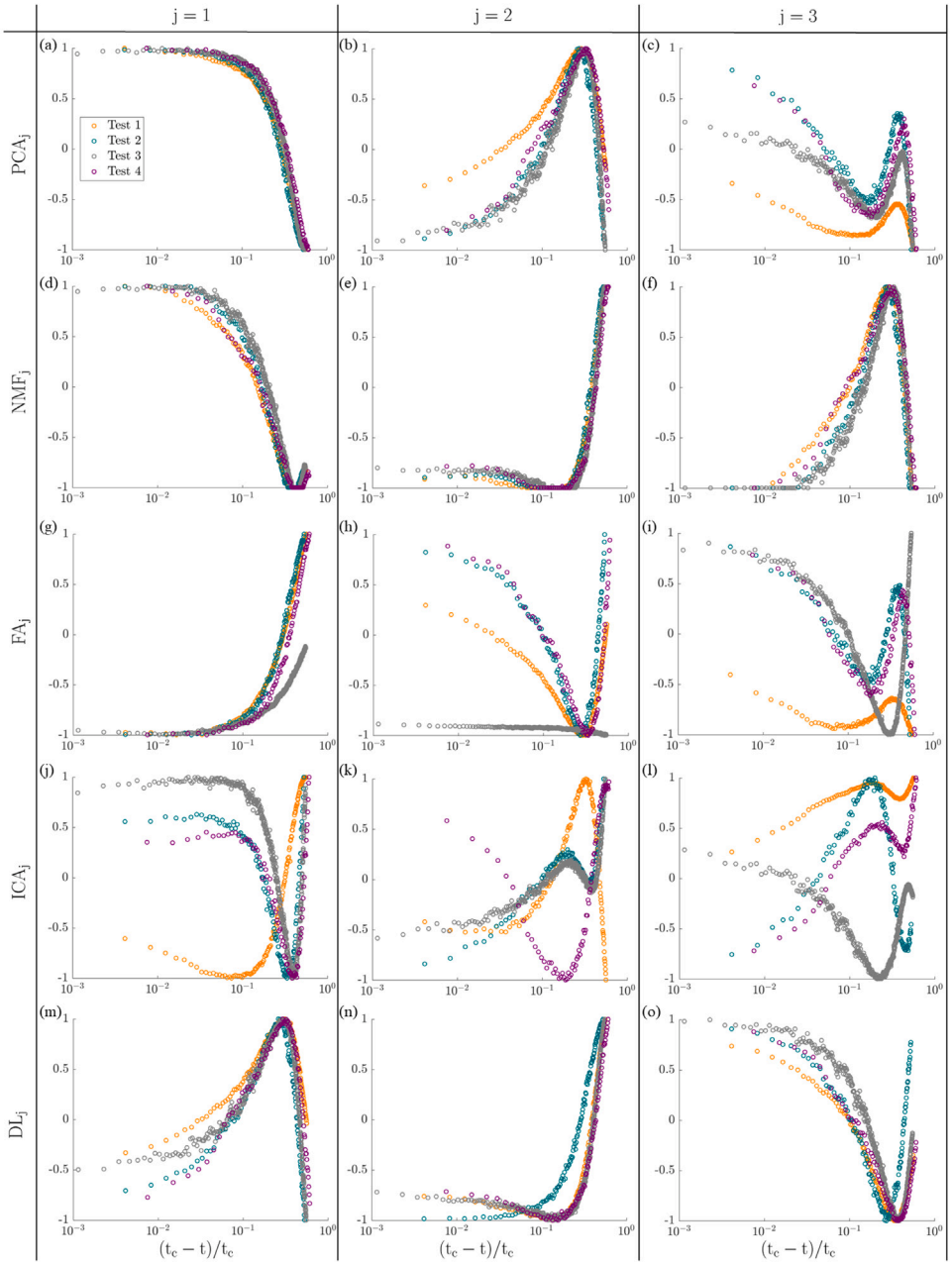

Fig. 3. The tabular figure displays the plots of the three components weight (indicated by column names) for the five-dimensionality reduction techniques (indicated by row names) across four experiments (a) PCA_1, (b) PCA_2, (c) PCA_3, (d) NMF_1, (e) NMF_2, (f) NMF_3, (g) FA_1, (h) FA_2, (i) FA_3, (j) ICA_1, (k) ICA_2, (l) ICA_3, (m) DL_1, (n) DL_2, (o) DL_3. The colors of the curves remain consistent across all figures for the experiments. The range of strain maps chosen corresponds to the range utilized in the improved PCA detection analysis (refer to Fig. 2) and is used to generate all components weight of the methods. Normalized components weight with the unit boundaries are plotted against normalized time before failure $(t_c - t)/t_c$. Note that time in these plots goes from right to left.

3c) displays two peaks: one maximum and one minimum. Notably, the transition from the maximum peak to the minimum peak occurs near the detection point of the second PCA component projection. Concerning the NMF components coefficient, the first NMF component coefficient (Fig. 3d) shows a transition from a low constant value to a high constant value, while the second NMF component coefficient (Fig. 3e) exhibits a transition from a high value to a constant low value around the peak position of the third component coefficient (Fig. 3f), which is used for detection. For the FA components score, the first FA component score (Fig. 3g) transitions from a high value to a low constant value, and the third FA component score (Fig. 3i) shows a transition from a maximum peak to a minimum peak (similar to the third PCA component projection) around the detection point of the minimum peak of the second FA component score (Fig. 3h), with one exception. As for the ICA components projection, the behavior appears experiment-dependent. The remaining ICA components projection, aside from those involved in peak detection, show either transitions from high to low values or transitions between two peaks around the detection point. Finally, for the DL components coefficient, the second DL component coefficient (Fig. 3n) transitions from a high value to a low value near the maximum peak position of the first DL component coefficient (Fig. 3m), while the third DL component coefficient (Fig. 3o) exhibits a minimum peak at the same position, which is used for detection.

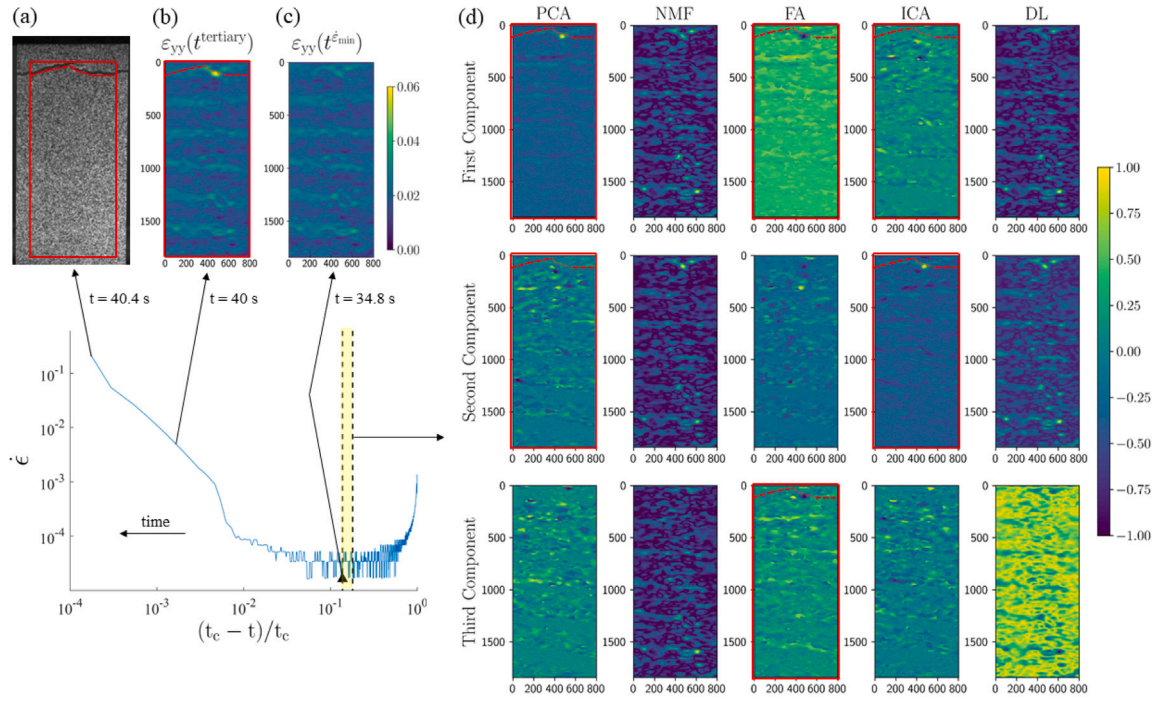

Fig. 4. An example experiment (Test 1) illustrating the ϵ_{yy} strain maps at two different deformation stages and component maps obtained through dimensionality reduction techniques, generated from a specific region of deformation. (a) Image of the material's crack surface at the sample failure moment. The red box indicates the Region of Interest (ROI) for the strain maps, and the dashed red line represents the crack path within this area. (b) ϵ_{yy} strain map during the tertiary creep deformation stage. (c) ϵ_{yy} strain map at the time of the minimum strain rate. (d) Component maps resulting from dimensionality reduction techniques, derived from fifty ϵ_{yy} strain maps up to the index corresponding to the minimum strain rate time. This range is highlighted with a yellow area on the curve. The crack path (red dashed line) is overlaid onto some of the component maps which show signatures of the failure of the sample, and onto the strain map at the tertiary creep regime.

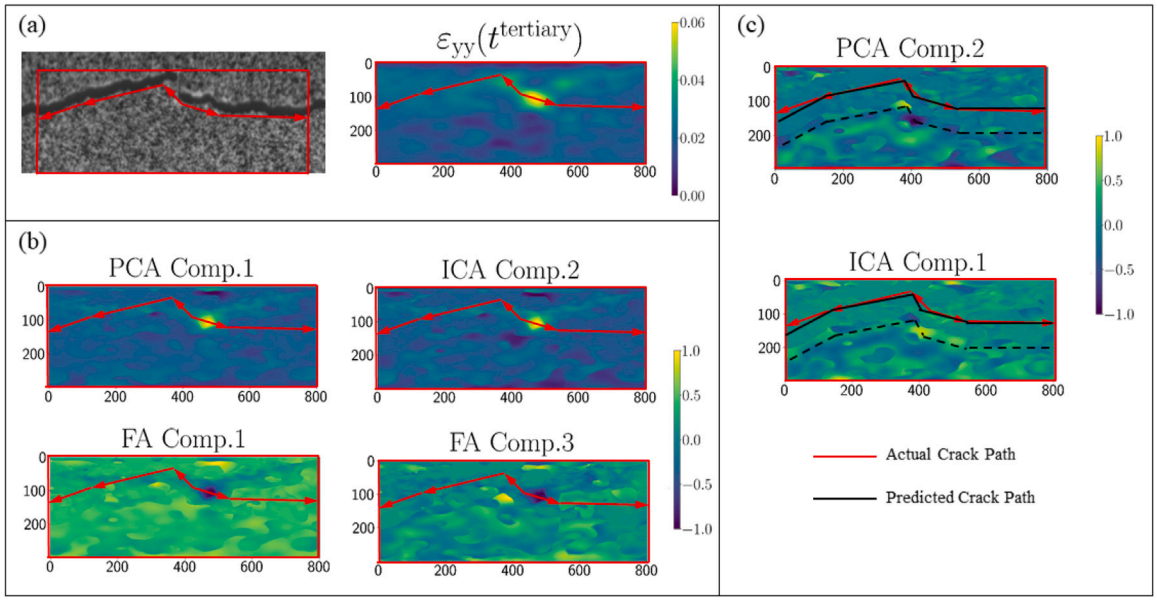

Fig. 5. Zoomed-in view around the crack path within the ROI area for selected maps from Fig. 4. (a) Red arrows indicate the direction of crack propagation, drawn on the crack surface and overlaid onto the ϵ_{yy} strain map at the tertiary creep phase, as well as onto the component maps in (b) and (c). (b) Component maps from three dimensionality reduction techniques (PCA, FA, and ICA) predict the final strain localization region through maximum and minimum hotspots. (c) Second PCA and first ICA component maps predict the entire crack path. The black dashed line represents the "separation path", marking the boundary between the uniform and patterned regions in the component maps, drawn slightly below this boundary for clarity. This dashed line is then shifted to align with the strain localization point predicted by other components (as seen in (b)), resulting in the solid black line that accurately represents the predicted crack path.

3.2. Prediction of the failure location

Predicting the localization of failure and the emergence of a final crack in a system without a dominant crack is a significant challenge. One of the initial approaches explored in previous studies involves analyzing the "activity spots" detected by DIC during early deformation stages, though these spots have not shown a strong correlation with the final deformation localization [18]. However, final failure localization becomes more apparent during the latest tertiary creep stage, as it results from a gradual evolution rather than a sudden

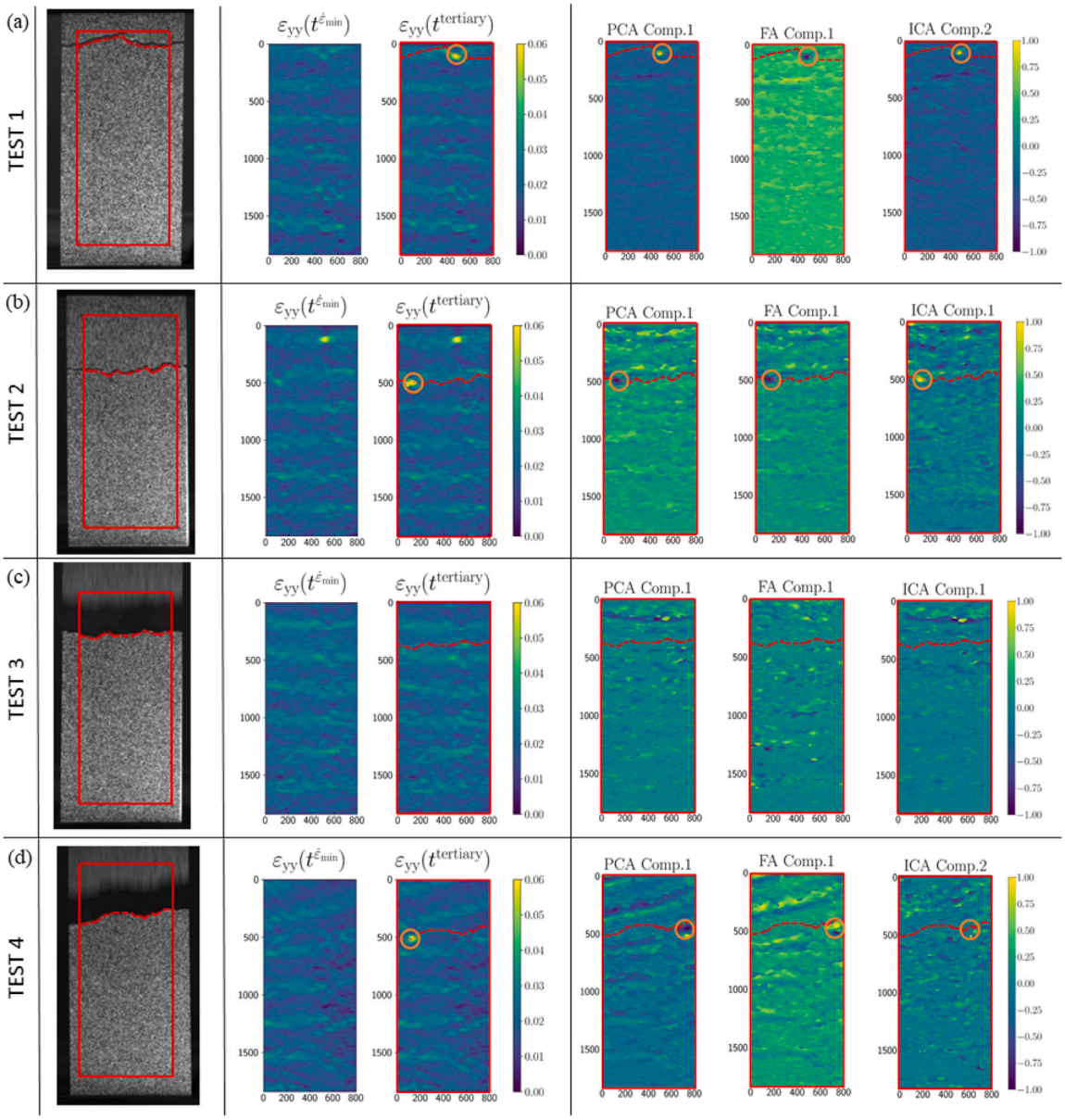

Fig. 6. The tabular figure demonstrates the same scenario as Fig. 4 but for all tests (a) 1, (b) 2, (c) 3, (d) (4). For each test, it shows the crack path inside the ROI area, strain maps at the time of minimum global strain rate, strain maps at tertiary creep deformation time (approximately 0.3 s before failure time), and the three most informative component maps (generated from 50 strain maps directly before the time of minimum global strain rate). The crack path is indicated with a red dashed line and is overlaid onto the strain maps at tertiary creep deformation time and onto the component maps. The orange empty circle indicates the location of the maximum or minimum hot spots of the maps. Component maps exhibit distinct patterns that consistently indicate the failure location across different experiments.

event in this phase of deformation [19]. Furthermore, evidence suggesting the predictability of failure time based on the critical level of accumulation of historical creep damage at the minimum strain rate level provides insights that the evolution of final deformation may commence relatively early, even close to the tertiary creep regime but not directly discernible on the local strain fields. Rather than examining a single strain map at a specific time, our method suggests producing a "characteristic image" of deformation through a set of strain maps that capture observed features across all spatial points over time. In this paper, these "characteristic images" are referred to as the "component maps" of the dimensionality reduction techniques.

We obtained the most informative component maps for predicting final deformation localization and crack path by utilizing 50 strain maps produced up to the time of the minimum global strain rate signal, starting about 1.7 s before t_{min}. In the example test case illustrated in Fig. 4, the prediction of failure location is achieved approximately 6 s before the failure time (or at 86% of the sample lifetime), providing a significant advancement in early and accurate forecasting of sample failure. However, strain localization can start to be visually detectable on local strain maps approximately 1 s before failure in the best-case scenario. In Fig. 4d, we demonstrate all three component maps of the five dimensionality reduction techniques. Upon careful examination of all 15 component maps, it is evident that three techniques (PCA, FA, and ICA) perform well in predicting the final failure location. In contrast, the remaining two techniques (NMF and DL) show early signs of hotspots in the strain maps, particularly in the bottom right regions; however, they are generally less informative for predicting final deformation. Notably, the second NMF map displayed a maximum at the final deformation localization in this experiment, but this observation was not consistent across other experiments.

In Fig. 5, we closely examine selected component maps from Fig. 4, which reveal signatures of the failure location. By zooming in on the

crack path region in these component maps, we make further observations about predicting the final strain localization point and the entire crack path within the ROI area. Notably, the first PCA and second ICA component maps predict the precise location of the final deformation localization with distinct maximum hotspots, while the first and third FA component maps indicate clear minimum hotspots (see Fig. 5b). Additionally, the second PCA and first ICA component maps predict the entire crack path (see Fig. 5c), displaying a relatively uniform, pattern-free area where the actual crack path, when overlaid, appears centrally within this region. The separation path between the uniform and patterned regions closely resembles the actual crack path. Aligning this separation path with the strain localization point predicted by other components enables an accurate prediction of the crack path.

In Fig. 6, we present the three most informative component maps for all four experiments, obtained from the three dimensionality reduction techniques (PCA, FA, and ICA), which demonstrated robust performance in predicting the final failure location. It is noteworthy that the first PCA and FA component maps consistently predict the failure location across all tests, whereas the predictive components in the ICA maps may vary between experiments. For clarity, the case of Test 1 (Fig. 6a) is illustrated in the previous Figs. 4, 5 and explained above. Similarly, for the other experiments, we generated component maps from the range of 50 strain maps just before the time of the minimum global strain rate ($t_{\min}$). In the case of Test 2 (Fig. 6b), two distinct strain localization hot spots are clearly observed on the strain map in the tertiary regime: one is located at the top of the map, while the other is positioned underneath it on the left side. Notably, the top hot spot is also visible on the strain map at the time of $t_{\min}$, whereas the other hot spot, from which the crack initiates, is not apparent at that time. However, the component maps predict the location of the main strain localization where the sample fractures with clear minimum (for PCA and FA) and maximum (for ICA) points on them. Moreover, the crack path surrounds the region with a stripe of minimum points (for PCA and FA) and maximum points (for ICA) on the component maps. This stripe originates from the most distinctly defined minimum and maximum points, establishing a clear trajectory. In the case of Test 3 (Fig. 6c), there is no strain localization at the end stage of the deformation, possibly due to the formation of a shear band and the uniform distribution of failure stress along the crack path. Consequently, the component maps do not show clear maximum or minimum points; instead, a uniform pattern-free area is observed on the component maps, overlapping with the crack path (notably, this uniform area is consistently observed on all three component maps of PCA, FA, and ICA for this experiment). Regarding the case of Test 4 (Fig. 6d), a coupling of the minimum and maximum hot spots of the first component maps of PCA and FA is located on the crack path but on the opposite side (right) of where the final deformation localization occurs (left side). This coupling would be a clear sign of the specific crack propagation like phenomena, where the flow of deformation starts from the right side and then localizes at the left side after the $t_{\min}$ time. Notably, in this experiment, the predictive ICA map is the second component, where the entire crack path is observable with a small uniform area, and the maximum is located near the right side around the crack path.

3.3. Comparison of dimensionality reduction techniques

In the first results sub-section, we identified optimal ranges of strain maps for detecting tertiary creep onset (the time of the minimum strain rate, $t_{\min}$). Using the strain maps from these ranges as input for dimensionality reduction techniques, we analyzed three components weight (projection, coefficient, or score of the components) and defined the corresponding specific component weight for each DR technique to detect $t_{\min}$. The results are discussed in the sub-section and presented in Table 1. Although we have a small sample size, overall, PCA, FA, and DL show consistent results with less variability, while NMF and ICA exhibit greater fluctuations, as indicated by their higher standard deviations (STD) and coefficients of variation (CV) calculated from the average values across four tests. This observed variability can be traced back to the intrinsic mathematical properties of the methods. PCA and FA prioritize variance maximization and modeling of the covariance structure, respectively, both of which focus on capturing dominant and robust features of the data, leading to their stable behavior across different samples. In contrast, ICA seeks to find statistically independent components, making it highly sensitive to noise and minor fluctuations in the data, as reported in resting-state fMRI studies [68], supporting our observations in strain field analysis. Even subtle differences across samples can lead ICA to different independent component solutions, which explains the greater sample-to-sample variation observed in our results. Similarly, NMF introduces additional variability due to its non-negativity constraint and its strong dependence on the initial conditions of the optimization; different initializations can cause NMF to converge to different local minima, as highlighted in muscle synergy extraction studies [69]. DL, while also a matrix factorization method, showed relatively more stable behavior compared to NMF, likely because its sparsity constraint forces the extracted components to focus on dominant localized patterns, thereby reducing sensitivity to noise and initialization variability. These considerations explain the strengths and weaknesses observed across the dimensionality reduction methods in predicting failure timing and localization. Despite these method-specific differences, it is noteworthy that under certain conditions, multiple techniques still produced closely aligned results. Interestingly, in some tests, the results from PCA, NMF, and FA are identical, suggesting a possible universal characteristic in the evolution of strain fields, where the time of failure can be predicted at approximately 70% of the sample lifetime.

In the second results sub-section, similar to the first, we analyzed the top three components of the DR methods. By deriving the components from the specific range of strain maps close to the time of the minimum global strain rate (tertiary creep onset), we reshaped the component vectors to match the size of the strain maps. Among all the techniques, PCA, FA, and ICA demonstrated the potential to predict the failure location. By examining the three component maps for each technique, we found that several components were informative. When a localization point was identified in one component map, examining the same location in another map could even reveal the signature of the entire crack path, even if the localization was not directly observable.

In the previous sub-sections, we compared the performance of the DR techniques based on the functionality of their specific components. However, to provide a more comprehensive assessment of these techniques, it is essential to consider the contribution of the top three components presented separately in the results. By taking into account the contributions of all three components, we can reconstruct the strain maps from the dimensionally-reduced spaces (refer to Eqs. (5), (7), (10), (12), (14)). As shown in Fig. 7, we may assess the ability of these techniques to capture the key features of the original data by comparing the differences between processed original strain maps X_k and the reconstructed strain maps $\hat{X}_k$ at the kth time step, given the chosen dimensional reduction. To ensure a clear and standardized comparison, the mean and standard deviation of these differences are normalized by the average strain maps $\langle X_k \rangle$ and plotted as a function of normalized time t/t_c with the failure time t_c, during creep testing. This approach helps to highlight the techniques' ability to approximate the original strain data over time, with lower mean differences and standard deviations in Fig. 7 signifying better dimensional reduction technique's performance.

In Fig. 7, the original and reconstructed strain maps used to compute the differences are selected from the same optimal range identified in the first results sub-section, where the input strain maps for the DR techniques were used to detect the onset of tertiary creep. At first glance, we can see that the mean differences across all tests remain close to zero for most of the deformation process but increase significantly near the failure time. To ensure a clearer visual comparison across tests, the y-axis limits were adjusted to focus on the main range

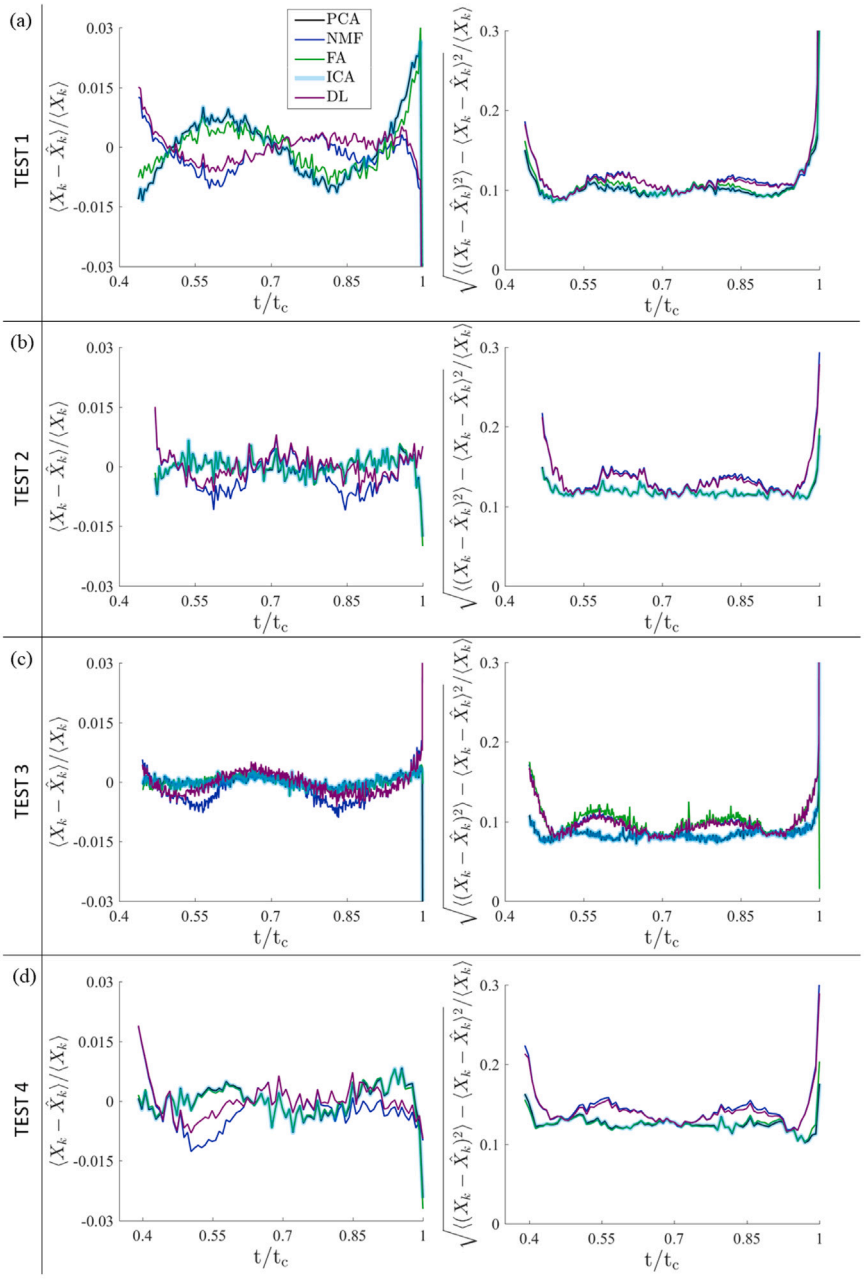

Fig. 7. The tabular figure presents the plots of the mean (first column) and standard deviation (second column) of the differences between the normalized original strain maps X_k (refer to Eq. (1)) and reconstructed strain maps $\hat{X}_k$ (refer to Eqs. (5), (7), (10), (12), (14)) for tests (a) 1, (b) 2, (c) 3, (d) 4, across five dimensionality reduction techniques. The colors of the curves are consistent across all figures for the DR techniques. The range of the original and reconstructed strain maps corresponds to the range used in Fig. 3. The mean and standard deviation of the differences are divided by the average of the processed strain maps $\langle X_k \rangle$ and plotted against the normalized time t/t_c.

of variation and avoid distraction from large fluctuations occurring at failure. These observations suggest that, overall, the DR techniques effectively capture the main features of the original data when using the top three components. However, the standard deviation plots reveal that NMF and DL exhibit slightly higher deviations, showing similar behavior across all tests. In contrast, PCA, ICA, and FA display lower deviations, with PCA and ICA producing nearly identical results. These lower deviations indicate that PCA, FA, and ICA perform better, as their mean differences are closer to zero, which also aligns with their success in predicting failure locations. An interesting observation from the plots across all the techniques is that the fluctuations tend to converge to zero mean differences and the curves overlap around the normalized time $t/t_c = 0.7$, corresponding to the detected onset of tertiary creep identified through dimensionality reduction techniques.

Overall, a valuable finding from an engineering perspective is that more than two dimensionality reduction techniques produce similar results. This is evident in Fig. 7, where the results from three techniques—PCA, ICA, and FA—as well as from two techniques—NMF and DL—show similar behavior. Additionally, at specific time steps, all the curves overlap, and the mean of the differences approaches zero. This overlap may explain why, in Table 1, we observe identical results in the detected onset of tertiary creep for PCA, NMF, and FA. All of these observations support the existence of universal characteristics in the evolution of local strain fields, providing a valuable framework for studying material mechanics from this perspective. Importantly, these findings enable significant predictions related to material failure, highlighting the practical applications of these techniques.

4. Discussion

We investigated the detection of the onset of tertiary creep failure and the prediction of the final deformation location by identifying universal features in the evolution of local strain fields obtained from DIC. By applying dimensionality reduction techniques as a form of unsupervised machine learning, we extracted and analyzed these features. Our developed methodology produced two types of results after reducing the matrix containing the strain maps throughout the deformation process: one in the form of a single curve and another as a single map representing the main characteristic of the evolution of the local strain fields.

By utilizing strain maps from the beginning of primary creep until failure as input for PCA analysis, we observed a peak in the second component projection around the time when the global strain rate signals started to plateau. This observation suggested easier detection of the onset of secondary creep compared to the challenging detection of the transition from the primary to secondary creep phase in noisy global strain rate signals. However, the main objective was to detect the onset of tertiary creep, as this stage represented the acceleration towards sample failure and served as a failure precursor, defined by the time of minimum global strain rate. To achieve this, we used strain maps from the time of secondary creep onset, as detected by PCA analysis, until failure for a new PCA analysis (referred to as improved PCA analysis). This approach resulted in improved detection of the onset of tertiary creep. Subsequently, we utilized the same range of strain maps from the improved PCA analysis as input for other dimensionality reduction techniques.

Despite differences in the working principles of the dimensionality reduction techniques, we observed that most of them identified the time values ($t_{\min}$) for the detection of tertiary creep onset, which, when normalized by the failure time t_c, appeared mostly identical (see Table 1). This finding suggests the presence of a universal characteristic in the evolution of local strain fields that facilitates the prediction of failure time. When comparing the average of the main ratio $t_{\min}/t_c$ across all tests, detected from global strain rate signals and with the application of dimensionality reduction techniques on the local strain data, we observed that the values showed less deviation from the average in the case of detection with dimensionality reduction techniques. Additionally, failure time could be predicted at 70% of the sample lifetime under static loading, preceding the prediction made by the Monkman-Grant relation (around 85% for the experiments in this study) for global strain data. Furthermore, from Fig. 2b (filled markers), it can be seen that even earlier predictions, around 40% of the sample lifetime, are possible by considering the secondary creep onset detected by PCA analysis. However, due to the limited number of samples, establishing strong statistical validity would require analyzing a larger number of experiments, which could be addressed in future studies.

Another significant discovery in this study was our ability to predict the location of failure (note that this approach is clearly different from segmentation of damage sites as presented e.g. in [45,46]) by using strain maps from the time range very close to the time of minimum global strain rate (onset of tertiary creep) to produce single "component maps". However, while the deformation (or strain) localization was not discernible on the strain map at the time of minimum global strain rate, these component maps from some dimensionality reduction techniques (PCA, FA, and ICA) showed clear signatures of the failure location (see Fig. 4). Our technique not only predicted the deformation localization point but also the entire crack path. As demonstrated in the example of Test 1, the first PCA, first and third FA, and second ICA component maps (see Fig. 5b) accurately predicted the location of strain localization. By examining the region around the strain localization point predicted by these components on the second PCA and first ICA component maps (see Fig. 5c), we identified a relatively uniform, pattern-free area. Adjusting the separation path between the uniform and patterned regions to align with the predicted strain localization point enabled an accurate prediction of the crack path.

Also, for the cases of the rest of the experiments (Fig. 6), we obtained insightful results. For example, if we observed two localization hotspots on the strain map from the early deformation stage, the technique selected the correct one where the sample fractured (as in the case of Test 2). If there was no localization point, the technique identified the crack path area as a uniform, pattern-free region (as in the case of Test 3). Additionally, if the technique revealed both maximum and minimum coupling of the hotspots on the component maps instead of a single hotspot, it appeared on the opposite side of the strain localization point but on the crack path (as in the case of Test 4). All of these findings for different cases showed that our technique had the power to reveal the signature of failure independent of the deformation phenomena and provided accurate predictions of failure location.

We provided an overall assessment of the dimensionality reduction techniques in Fig. 7 by considering the contributions of the top three components. Strain maps were reconstructed from dimensionally reduced spaces and subtracted from the original strain maps. By examining the mean and standard deviation of the differences, we found that techniques such as PCA, ICA, and FA performed better, as their standard deviations were lower and mean differences were closer to zero, and they excelled in predicting failure locations on the material surfaces. Interestingly, at specific time steps, the curves of all techniques overlapped around the zero mean differences, with one of these steps aligning with the detection of tertiary creep. Although NMF and DL exhibited higher deviations in the differences, they still provided reasonable and comparable results for detecting the onset of tertiary creep. We also note that, although ICA performed well in predicting failure locations on the material surface, it did not perform as effectively in detecting the onset of tertiary creep. The values showed noticeable deviations from the average across the experiments and also from the results of the other techniques (see Table 1). Among the dimensionality reduction techniques, ICA exhibited greater sample-to-sample variability because it seeks statistically independent components, making it highly sensitive to noise and subtle differences across datasets. NMF, on the other hand, showed variability due to its dependence on initialization and its non-negativity constraint, which can cause convergence to different local minima. These intrinsic characteristics explain why PCA and FA, which prioritize capturing dominant variations in a more stable manner, outperformed the others in both detecting tertiary creep onset and predicting failure locations. In conclusion, based on the overall assessment of the five techniques, we conclude that PCA and FA performed better in both detecting tertiary creep onset and predicting failure locations.

In this study, we conducted a limited number of experiments, as our main objective was to demonstrate the practicality of applying dimensionality reduction techniques to the analysis of local strain data for studying the creep mechanics of materials. By applying five different dimensionality reduction techniques, we demonstrated their effectiveness, and, through obtaining similar results from most of them, we highlighted a valuable finding: the presence of universal characteristics in the evolution of local strain fields. These characteristics can be revealed and utilized for precise failure prediction through our novel framework. While this study focused on a small sample size, future work will involve increasing the number of experiments to further validate these findings and explore the broader applicability of these techniques.

The present article investigated paper and an example of a quasi-brittle composite material. This group includes important structural materials such as concrete [70], mortar [71], ceramics [72], rocks [73,74] and some FRP composites [75]. Moreover, paper has a master curve creep behavior similar to many other materials and thus can be considered as a model material [76]. While the current dataset has been limited to paper samples, the dimensionality reduction techniques used are not material-specific. Rather, they operate purely on the structure of strain fields, making them applicable across materials where deformation fields can be measured. For instance, PCA has been applied in previous work to DIC strain maps obtained from uniaxial tension tests of nickel-based alloys (cf. [20]). This example demonstrates that DR techniques can be successfully applied not only to other quasi-brittle materials, but also to metals and alloys.

5. Conclusions

In this study, we developed a methodology based on dimensionality reduction techniques to extract universal features from the evolution of local strain fields during creep deformation. By analyzing the strain field evolution with five different techniques, we demonstrated that it is possible to detect the onset of tertiary creep and to predict the failure time. Our approach enabled the robust prediction of deformation localization and the early identification of crack paths well before macroscopic localization became visible. These findings highlight the effectiveness of dimensionality reduction techniques in advancing the understanding and prediction of material failure phenomena.

In this research, we used quasi-brittle paper samples to study creep phenomena through the analysis of local strain fields. While paper's creep behavior is similar to that of engineering materials, it has a much higher creep rate and a shorter secondary creep phase. These findings motivate further studies on other materials, such as ductile metals, which have longer creep phases and require extended testing times [12,77]. Our developed techniques can be applied to these materials, offering early failure predictions. A key advantage is that failure prediction relies solely on DIC strain maps, making it applicable to components in operating systems where traditional mechanical testing is impractical. By using surface images alone, weak regions can be identified and reinforced, extending the lifespan of these components.

CRediT authorship contribution statement

Bakhtiyar Mammadli: Writing – review & editing, Writing – original draft, Visualization, Methodology, Investigation, Formal analysis, Data curation. **Tero Mäkinen:** Writing – review & editing, Visualization, Data curation. **Karol Frydrych:** Writing – review & editing, Writing – original draft. **Panagiotis G. Asteris:** Writing – review & editing, Methodology. **Stefanos Papanikolaou:** Writing – review & editing, Supervision, Project administration, Methodology, Funding acquisition, Conceptualization.

Declaration of competing interest

The authors declare that they have no known competing financial interests or personal relationships that could have appeared to influence the work reported in this paper.

Acknowledgments

The publication was created within the framework of the project of the Minister of Science and Higher Education "Support for the activities of Centres of Excellence established in Poland under Horizon 2020" under contract no. MEiN/2023/DIR/3795. We acknowledge the computational resources provided by the National Centre for Nuclear Research in Poland. T.M. acknowledges support from the FinnCERES flagship (grant no. 151830423), Business Finland (grant nos. 211835, 211909, and 211989), and Future Makers programs. We also acknowledge the Complex Systems and Materials (CSM) lab at the Department of Applied Physics, Aalto University, Finland, for their support with the experiments.

Appendix. Effect of the averaging window on the minimum strain rate time

To quantitatively assess the robustness of minimum strain rate detection, we analyzed the effect of different averaging window sizes applied to the global strain rate signals. Fig. 8 illustrates the outcome for a representative experiment (Test 1). As shown in Fig. 8a, applying a large averaging window (1400 datapoints, corresponding to 14 s) effectively suppresses noise and reveals a distinct single minimum in the strain rate signal, corresponding to the onset of tertiary creep.

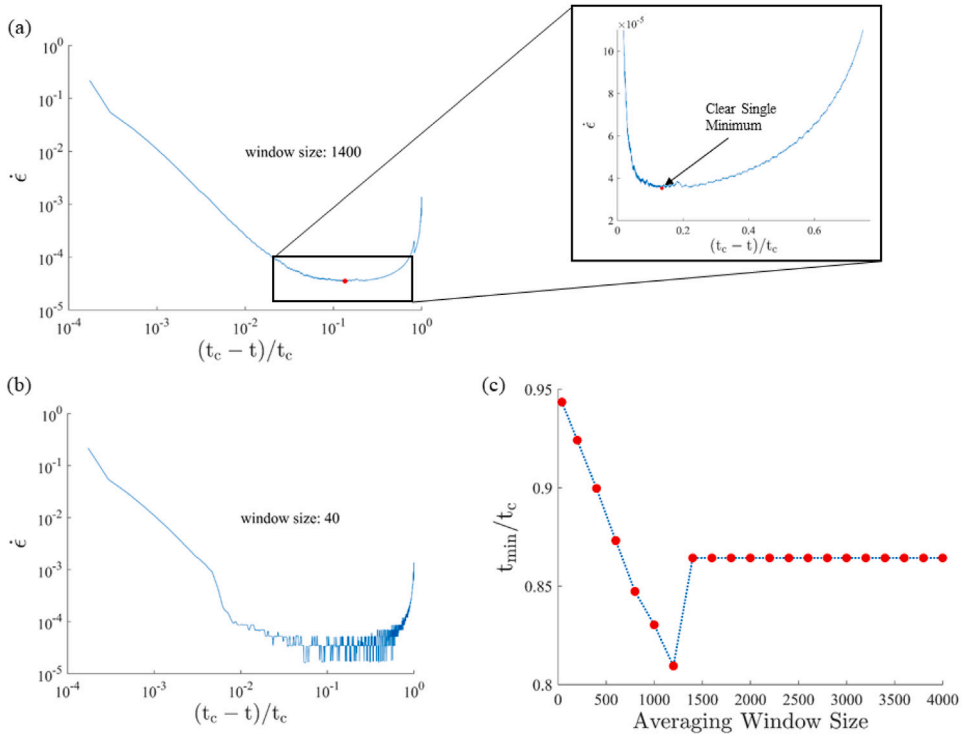

Fig. 8. Robust identification of the minimum strain rate time t_{min} from global strain rate ($\dot{\epsilon}$) signals demonstrated using data from Test 1. (a) Smoothed global strain rate curve obtained with a large averaging window size of 1400 data points, revealing a clear single minimum (marked in red), which corresponds to the onset of the tertiary creep phase. The inset highlights this well-defined minimum in linear scale. (b) Corresponding curve using a smaller window size of 40 points, which better visualizes the creep phases but retains more noise. This window size is used in Figs. 2 and 4. Note that in both plots (a) and (b), time goes from right to left. (c) Normalized minimum strain rate time (t_{min}/t_c) plotted against varying averaging window sizes. Beyond a threshold (around 1400 points), the detected t_{min} stabilizes, confirming the robustness of the method.

In contrast, Fig. 8b demonstrates that while a smaller window size (40 points) retains more noise, it enables the visualization of the full creep behavior, including transitions between primary, secondary, and tertiary phases.

To further evaluate the sensitivity of the detected minimum, we plotted the normalized minimum time (t_{min}/t_c) against a range of averaging window sizes in Fig. 8c. The results show that once the window size exceeds a certain threshold (around 1400 datapoints), the detected t_{min} remains constant despite further increases in smoothing. This confirms that the proposed approach provides a robust and reproducible method for identifying the onset of tertiary creep in noisy experimental signals.

Data availability

The data used in this study are available on Zenodo: https://doi.org/10.5281/zenodo.15554332.

References

[1] Kowalewski ZL, Ustrzycka A. Creep deformation. Encycl Contin Mech 2020;499–508.
[2] Zhong Y, Lai HS, Guo J, Du P, Huang Q. Small punch test for investigating circumferential creep in cladding tubes. Int J Mech Sci 2024;267:109001.
[3] Li J, Liu Z, Liu M, Kuang Y, Zhang Z, Chen X. Temperature-dependent creep damage mechanism and prediction model of fiber-reinforced phenolic resin composites. Int J Mech Sci 2024;109477.
[4] Huang L, Sauzay M, Cui Y, Bonnaille P. Theoretical and experimental study of creep damage in alloy 800 at high temperature. Mater Sci Eng: A 2021;813:140953.
[5] Lo Frano R, Cancemi SA, Darnowski P, Ciolini R, Paci S. Preliminary analysis of an aged RPV subjected to station blackout. Energies 2021;14(15):4394.
[6] Ridley M, Massey C, Bell S, Capps N. High temperature creep model development using in-situ 3-D DIC techniques during a simulated LOCA transient. Ann Nucl Energy 2023;193:110012.
[7] Wen Z, Liang J, Liu C, Pei H, Wen S, Yue Z. Prediction method for creep life of thin-wall specimen with film cooling holes in Ni-based single-crystal superalloy. Int J Mech Sci 2018;141:276–89.
[8] Gu S, Gao H, Wen Z, Li Z, Zhang C, Yue Z. Creep properties and life model of anisotropic Ni-based single crystal superalloys over a wide temperature range. Int J Mech Sci 2024;261:108674.
[9] Cheng L-Y, Wang R-Z, Wang J, Zhu S-P, Zhao P-C, Miura H, Zhang X-C, Tu S-T. Cycle-dependent creep-fatigue deformation and life predictions in a nickel-based superalloy at elevated temperature. Int J Mech Sci 2021;206:106628.
[10] Mäkinen T, Tuokkola L, Lahikainen J, Lomakin IV, Koivisto J, Alava MJ. Crack propagation by activated avalanches during creep and fatigue from elastic interface theory. Phys Rev Lett 2025;134(9):098202.
[11] Qin R, Li Y, Wong SY, Teo FY, Yu Z, Sun L, Zheng Y. Understanding on the creep behavior of fiber reinforced polymer via fiber/matrix interaction. Constr Build Mater 2024;451:138875.
[12] Kimura K, Sawada K, Kushima H, Toda Y. Influence of chemical composition and heat treatment on long-term creep strength of grade 91 steel. Procedia Eng 2013;55:2–9.
[13] Mach RM. An accelerated creep testing program for nickel based superalloys (Ph.D. thesis), The University of Texas at El Paso; 2020.
[14] Ayubali AA, Singh A, Shanmugavel BP, Padmanabhan K. A phenomenological model for predicting long-term high temperature creep life of materials from short-term high temperature creep test data. Int J Mech Sci 2021;202:106505.
[15] Verano-Espitia JC, Weiss J, Amitrano D, Mäkinen T, Alava M. Effect of quenched heterogeneity on creep lifetimes of disordered materials. Phys Rev E 2024;110(6):064133.
[16] Mäkinen T, Weiss J, Amitrano D, Roux P. History effects in the creep of a disordered brittle material. Phys Rev Mater 2023;7(3):033602.
[17] Alava M, Niskanen K. The physics of paper. Rep Progr Phys 2006;69(3):669.
[18] Koivisto J, Ovaska M, Miksic A, Laurson L, Alava MJ. Predicting sample lifetimes in creep fracture of heterogeneous materials. Phys Rev E 2016;94(2):023002.
[19] Mäkinen T, Koivisto J, Laurson L, Alava MJ. Scale-free features of temporal localization of deformation in late stages of creep failure. Phys Rev Mater 2020;4(9):093606.
[20] Mäkinen T, Zaborowska A, Frelek-Kozak M, Jóźwik I, Kurpaska Ł, Papanikolaou S, Alava MJ. Detection of the onset of yielding and creep failure from digital image correlation. Phys Rev Mater 2022;6(10):103601.
[21] Pournajar M, Mäkinen T, Hosseini SA, Moretti P, Alava M, Zaiser M. Failure precursors and failure mechanisms in hierarchically patterned paper sheets in tensile and creep loading. Phys Rev Appl 2023;20(2):024008.
[22] Rios-Soberanis CR, Cruz-Estrada RH, Rodriguez-Laviada J, Perez-Pacheco E. Study of mechanical behavior of textile reinforced composite materials. Dyna 2012;79(176):115–23.
[23] Andrade ENDC. On the viscous flow in metals, and allied phenomena. Proc R Soc Lond A 1910;84:1–12.
[24] Cottrell AH. Logarithmic and andrade creep. Phil Mag Lett 1997;75(5):301–8.
[25] Rosti J, Koivisto J, Laurson L, Alava MJ. Fluctuations and scaling in creep deformation. Phys Rev Lett 2010;105:100601.
[26] Monkman FC, Grant NJ. An empirical relationship between rupture life and minimum creep rate in creep-rupture tests. ASTM Proc 1956;56:593–620.
[27] Goertzen WK, Kessler M. Creep behavior of carbon fiber/epoxy matrix composites. Mater Sci Eng: A 2006;421(1–2):217–25.
[28] Hu H. Master curve of creep in polymeric off-axis composite laminates. J Mech 2006;22(3):229–34.
[29] Yang Z, Wang H, Ma X, Shang F, Ma Y, Shao Z, Hou D. Flexural creep tests and long-term mechanical behavior of fiber-reinforced polymeric composite tubes. Compos Struct 2018;193:154–64.
[30] Sakai T, Hirai Y, Somiya S. Estimating the creep behavior of glass-fiber-reinforced polyamide considering the effects of crystallinity and fiber volume fraction. Mech Adv Mater Mod Process 2018;4:1–9.
[31] Zhang Y-Y, Sun Z, Li Y-Q, Huang P, Chen Q, Fu S-Y. Tensile creep behavior of short-carbon-fiber reinforced polyetherimide composites. Compos Part B: Eng 2021;212:108717.
[32] Prakash A, Sandfeld S. Chances and challenges in fusing data science with materials science. Pr Met 2018;55(8):493–514.
[33] Rodrigues JF, Florea L, de Oliveira MC, Diamond D, Oliveira ON. Big data and machine learning for materials science. Discov Mater 2021;1:1–27.
[34] Pilania G. Machine learning in materials science: From explainable predictions to autonomous design. Comput Mater Sci 2021;193:110360.
[35] Frydrych K, Karimi K, Pecelerowicz M, Alvarez R, Dominguez-Gutiérrez FJ, Rovaris F, Papanikolaou S. Materials informatics for mechanical deformation: A review of applications and challenges. Materials 2021;14(19):5764.
[36] Papadimitriou I, Gialampoukidis I, Vrochidis S, Kompatsiaris I. AI methods in materials design, discovery and manufacturing: A review. Comput Mater Sci 2024;235:112793.
[37] Benzaamia A, Ghrici M, Rebouh R, Pilakoutas K, Asteris PG. Predicting the compressive strength of CFRP-confined concrete using deep learning. Eng Struct 2024;319:118801.
[38] Deshpande S, Rappel H, Hobbs M, Bordas SP, Lengiewicz J. Gaussian process regression+ deep neural network autoencoder for probabilistic surrogate modeling in nonlinear mechanics of solids. Comput Methods Appl Mech Engrg 2025;437:117790.
[39] Wang X, Yang J, Chen H, Xuan F. Physics-based probabilistic assessment of creep-fatigue failure for pressurized components. Int J Mech Sci 2023;250:108314.
[40] Liu C, Shi D, Zhang B, Yang X, Chen H. A novel creep-fatigue life evaluation method for ceramic-composites components. Int J Mech Sci 2023;249:108259.
[41] Kowalewski ZL, Ustrzycka A, Szymczak T, Makowska K, Kukla D. Damage identification supported by nondestructive testing techniques. Plast Damage Fract Adv Mater 2020;67–117.
[42] Leygue A, Coret M, Réthoré J, Stainier L, Verron E. Data-based derivation of material response. Comput Methods Appl Mech Engrg 2018;331:184–96.
[43] Kirchdoerfer T, Ortiz M. Data-driven computational mechanics. Comput Methods Appl Mech Engrg 2016;304:81–101.
[44] Cidade RA, Castro DS, Castrodeza EM, Kuhn P, Catalanotti G, Xavier J, Camanho PP. Determination of mode I dynamic fracture toughness of IM7-8552 composites by digital image correlation and machine learning. Compos Struct 2019;210:707–14.
[45] Rezaie A, Achanta R, Godio M, Beyer K. Comparison of crack segmentation using digital image correlation measurements and deep learning. Constr Build Mater 2020;261:120474.
[46] Perera R, Huerta MC, Barris C, Baena M. Clustering classifier of FRP strengthened concrete beams using superpixels and principal component analysis. Constr Build Mater 2024;453:139019.
[47] Min H-G, On H-I, Kang D-J, Park J-H. Strain measurement during tensile testing using deep learning-based digital image correlation. Meas Sci Technol 2019;31(1):015014.
[48] Boukhtache S, Abdelouahab K, Berry F, Blaysat B, Grediac M, Sur F. When deep learning meets digital image correlation. Opt Lasers Eng 2021;136:106308.
[49] Yang R, Li Y, Zeng D, Guo P. Deep DIC: Deep learning-based digital image correlation for end-to-end displacement and strain measurement. J Mater Process Technol 2022;302:117474.
[50] Archana R, Jeevaraj PE. Deep learning models for digital image processing: a review. Artif Intell Rev 2024;57(1):11.
[51] Cheng X, Ma Q, Zhou S, Guo L, Ma S. Using unsupervised learning based convolutional neural networks to solve digital image correlation. Opt Laser Technol 2025;180:111414.
[52] Yang J, Bhattacharya K. Augmented Lagrangian digital image correlation. Exp Mech 2019;59:187–205.

[53] Lomakin IV, Mäkinen T, Widell K, Savolainen J, Coffeng S, Koivisto J, Alava MJ. Fatigue crack growth in an aluminum alloy: Avalanches and coarse graining to growth laws. Phys Rev Res 2021;3(4):L042029.
[54] Wold S, Esbensen K, Geladi P. Principal component analysis. Chemometr Intell Lab Syst 1987;2(1–3):37–52.
[55] Papanikolaou S, Alava MJ. Direct detection of plasticity onset through total-strain profile evolution. Phys Rev Mater 2021;5(8):083602.
[56] Papanikolaou S. An informatics method for inferring the hardening exponent of plasticity in polycrystalline metals from surface strain measurements. J Mater Sci: Mater Theory 2024;8(1):1.
[57] Minka T. Automatic choice of dimensionality for PCA. In: Leen T, Dietterich T, Tresp V, editors. Advances in neural information processing systems. Vol. 13, MIT Press; 2000.
[58] Sra S, Dhillon I. Generalized nonnegative matrix approximations with Bregman divergences. Adv Neural Inf Process Syst 2005;18.
[59] Cichocki A, Phan A-H. Fast local algorithms for large scale nonnegative matrix and tensor factorizations. IEICE Trans Fundam Electron Commun Comput Sci 2009;E92.A(3):708–21.
[60] Févotte C, Idier J. Algorithms for Nonnegative Matrix Factorization with the β-Divergence. Neural Comput 2011;23(9):2421–56.
[61] Kline P. An easy guide to factor analysis. Routledge; 2014.
[62] Barber D. Bayesian reasoning and machine learning. Cambridge University Press; 2007, p. 389–91.
[63] Bishop CM. Pattern recognition and machine learning. Springer; 2006, p. 583–6.
[64] Lee T-W. Independent component analysis. In: Independent component analysis: theory and applications. Springer; 1998, p. 27–66.
[65] Hyvärinen A, Oja E. Independent component analysis: algorithms and applications. Neural Netw 2000;13(4):411–30.
[66] Tošić I, Frossard P. Dictionary learning. IEEE Signal Process Mag 2011;28(2):27–38.
[67] Mairal J, Bach F, Ponce J, Sapiro G. Online dictionary learning for sparse coding. In: Proceedings of the 26th annual international conference on machine learning. 2009, p. 689–96.
[68] Risk BB, Kociuba MC, Rowe DB. An evaluation of independent component analyses with an application to resting-state fMRI. Biometrics 2014;70(1):224–36.
[69] Ebied A, Kinney-Lang E, Steele C, Holmes M, Escudero J. Evaluation of matrix factorisation approaches for muscle synergy extraction. Med Eng Phys 2018;57:63–73.
[70] Vilppo J, Kouhia R, Hartikainen J, Kolari K, Fedoroff A, Calonius K. Anisotropic damage model for concrete and other quasi-brittle materials. Int J Solids Struct 2021;225:111048.
[71] Pichler B, Hellmich C. Upscaling quasi-brittle strength of cement paste and mortar: A multi-scale engineering mechanics model. Cem Concr Res 2011;41(5):467–76.
[72] Sadowski T. Modelling of semi-brittle ceramics behaviour under a quasi-static deformation process. In: IUTAM symposium on anisotropy, inhomogeneity and nonlinearity in solid mechanics: proceedings of the IUTAM-iSIMM symposium held in nottingham, UK, 30 August–3 September 1994. Springer; 1995, p. 281–6.
[73] Kornev V, Zinov'ev A. Quasi-brittle rock failure model. J Min Sci 2013;49:576–82.
[74] Gheibi S, Holt RM. Fracture assessment of quasi-brittle rock simulated by modified discrete element method. Rock Mech Rock Eng 2020;53(8):3793–805.
[75] Han Z, Qu W, Zhu P. Tensile behavior of GFRP bar at quasi-static and high strain rate. Constr Build Mater 2023;364:129915.
[76] Villette F, Baroth J, Dufour F, Rolland du Roscoat S. Displaying quasi-brittle failure using avalanches: paper as a material model. Int J Fract 2024;245(1):25–35.
[77] Wang Y, Zhang W, Wang Y, Lim YC, Yu X, Feng Z. Experimental evaluation of localized creep deformation in grade 91 steel weldments. Mater Sci Eng: A 2021;799:140356.